Submitted for the proceedings of the Sentinel-2 for Science Workshop
held in Frascati, Italy, 20-23 May 2014, ESA Special Publication SP-726

ATMOSPHERIC CORRECTION OF LANDSAT-8 IMAGERY USING SEADAS

Quinten Vanhellemont[(1)], Sean Bailey[(2)], Bryan Franz[(2)], Don Shea[(2)]

[(1)] Royal Belgian Institute of Natural Sciences (RBINS), Operational Directorate Natural Environment, Gulledelle 100, 1200 Brussels E-mail: q.vanhellemont@mumm.ac.be
[(2)] Ocean Biology Processing Group (OBPG), NASA/Goddard Space Flight Center, Greenbelt, Maryland 20771, USA

ABSTRACT

Here we present the implementation of the atmospheric correction of Landsat-8/OLI imagery in SeaDAS/l2gen, which will make Landsat-8 processing accessible to a wider audience in a standardized sensor-generic and well-supported system. A comparison is made between the processing of Vanhellemont and Ruddick (2014) and SeaDAS for several scenes in Belgian waters. Marine spectra from three images compare well with in situ Aeronet-OC measurements. This exercise is an excellent preparation for Sentinel-2 processing that will be similarly implemented in SeaDAS.

1. INTRODUCTION

Wide-swath medium resolution (0.25 - 1 km) sensors such as MODIS, have been used for monitoring coastal and oceanic waters for over a decade. They offer an approximately daily revisit time, which is a vast improvement over traditional discrete in situ sampling campaigns. However, their spatial resolution is often insufficient in coastal waters and estuaries. High resolution sensors such as Landsat-8 (2013-…) and Sentinel-2 (to be launched) have the potential to observe the small scale spatial variability of coastal waters. The high resolution (30 m) Operational Land Imager (OLI) on Landsat-8 is a promising new data source for coastal research (spectral bands are given in Table 1). The imagery is freely available from USGS, and first results show that small scale features of suspended sediments in coastal waters can be reliably mapped (Vanhellemont and Ruddick, 2014).

2. METHODS

Level 1 imagery from the Operational Land Imager (OLI) on Landsat-8 was obtained in GeoTIFF format from EarthExplorer (http://earthexplorer.usgs.gov/) for three days (2014-03-16, 2014-04-01 and 2014-04-17) where the MOW1 platform (51.362°N; 3.120°E) near Zeebrugge harbour is cloud-free. Level 1 data from the Aeronet-OC station at MOW1 were obtained from the Aeronet website (http://aeronet.gsfc.nasa.gov/).

The atmospheric correction of Vanhellemont and Ruddick (2014), hereafter VR2014, corrects the imagery for Rayleigh and aerosol scattering. The Rayleigh correction has been updated and now uses a lookup table generated using 6SV (Vermote et al., 2006), as the analytical method proved to be unreliable at high sun zenith angles. The ratio of marine reflectances in the red and NIR bands, respectively ρ_w^4 and ρ_w^5, is assumed to be constant ($\alpha = 8.7$), which is generally valid for the turbidity levels observed in the Belgian coastal zone. The ratio of aerosol reflectances in the red and NIR bands (or aerosol type, ε) is assumed to be constant over the scene. Following the reasoning of Ruddick et al. (2000), the marine reflectance in the red band can be derived.

ε can be determined over clear water pixels or set to a regional value. Here, ε was set to the median ratio of Rayleigh corrected reflectances (ρ_c^4 / ρ_c^5) for clear water pixels in the scene. Clear water pixels were determined iteratively using a first guess of $\varepsilon = 1$ and a threshold on the resulting ρ_w^4 (< 0.005). Alternatively, the two SWIR bands can be used for aerosol determination, and no assumptions on the marine reflectances are required. A fixed per-scene ε is derived from the SWIR bands (Vanhellemont and Ruddick, in prep), hereafter referred to as VR2014-SWIR. ε was extrapolated to the visible channels using the exponential:

$$\varepsilon^{i,L} = \varepsilon^{S,L\ \delta i} \qquad (1)$$

where L and S are the longest (5, 6 or 7) and shortest (4, 5 or 6) wavelength bands used, i the band index, and

$$\delta i = \frac{\lambda_L - \lambda_i}{\lambda_L - \lambda_S} \qquad (2)$$

Standard SeaDAS/l2gen aerosol (eighty models: eight relative humidities and ten size fractions) and Rayleigh lookup tables were generated using the relative spectral response function of the OLI bands (Barsi et al., 2011). A data reader for the L1T files generated by the Level 1 Product Generation System (LGPS) was implemented and integrated in l2gen.

Three atmospheric corrections have been tried in l2gen, following the Gordon and Wang (1994) algorithm. Two approaches use different band combinations for aerosol type estimation: the NIR and SWIR1 bands (SD-NIR, 5 and 6) and SWIR1 and SWIR2 bands (SD-SWIR, 6 and 7). The iterative NIR model (Bailey et al., 2010) and BRDF correction (a.o. Morel and Gentili, 1996) have been disabled. The third one, SD-MUMM, is effectively a clone of the VR2014 processing, by using the Ruddick

et al. (2000) implementation in l2gen (option aer_opt=-10), using bands 4 and 5 and setting $\alpha = 8.7$. For all three methods, the aerosol radiance is extrapolated to the visible bands using the above-mentioned aerosol lookup tables. Remote sensing reflectance (Rrs) from the SeaDAS outputs is converted to marine reflectance ($Rrs = \rho_w / \pi$).

3. RESULTS

Maps of marine reflectance derived from the 2014-03-16 image and comparative scatterplots are given in Figure 1 for processors VR2014 and SD-NIR, in Figure 2 for VR2014 and SD-SWIR and in Figure 3 for VR2014 and SD-MUMM. The turbid waters of the Belgian coastal zone are characterised by high marine reflectances (ρ_w), especially in the green and red bands. Apart from the green band, the SD-NIR processor tends to give lower ρ_w than the VR2014 and VR2014-SWIR. The SD-SWIR and VR2014-SWIR give highest values overall. The pixelation on the coastline in the SeaDAS maps is caused by the coarse resolution of the used landmask. In the most turbid waters, the SeaDAS cloud flag is triggered (using the standard albedo threshold), and the VR2014 approach underestimates the marine signal due to the assumption of a constant ratio between ρ_w in the red and NIR bands.

A comparison with Level 1 Aeronet-OC normalised water-leaving radiance ($nLw = \pi \cdot \rho_w \cdot F0$) spectra is shown in Figure 4 for VR2014 and VR2014-SWIR, in Figure 5 for SD-NIR and SD-SWIR and in Figure 6 for VR2014 and SD-MUMM (with $\varepsilon = 1$). In general, the spectra are quite close to the Aeronet-OC spectra. A similar trend is seen across matchups, with the VR2014 overestimating, and the SD-NIR underestimating in comparison to the Aeronet-OC data. Also here it is clear that the SWIR based processors both give higher reflectances across the spectrum. A higher spatial variability is found in the SD-SWIR processing (vertical bars denote 10-90th percentile range), due to noise in the SWIR bands. This problem is partially avoided by the VR2014-SWIR correction by fixing the ε per scene.

4. DISCUSSION

In the Belgian coastal zone quite good agreements between the VR2014/VR2014-SWIR and the SD-NIR are found in the green and red bands. The VR2014 and VR2014-SWIR algorithms give slightly higher red ρ_w than the SD-NIR, and higher ρ_w than the SD-SWIR in two of the three matchups. In the green, the SD retrievals are higher for the two more turbid matchups (2014-03-16 and 2014-04-01). The worst comparison between SD-NIR and VR2014 and VR2014-SWIR and SD-SWIR is in the blue, where the VR2014 processing retrieves much higher values. As they are essentially using the same approach, VR2014 and SD-MUMM give very close results, with some deviation in the blue thanks to the differences in aerosol extrapolation.

A large part of the scatter in the comparison between SD and VR2014 – generally along a best-fit line - can be explained by the per-pixel varying aerosol model in SeaDAS. The slopes of the best-fit lines, or of the different branches in the point cloud, are mainly determined by the aerosol model selected by SeaDAS and by simplifications in the atmospheric transmittances by VR2014.

Realistic looking turbid water spectra are retrieved for the MOW1 station. In terms of spectral shape, agreement with the Aeronet-OC L1 data is good for all processors. In general the VR2014 approach has a relatively small overestimation in the visible channels, and the VR2014-SWIR has a larger overestimation across the VIS-NIR. These overestimations are probably caused by sensitivity to aerosol type estimation and aerosol extrapolation to the visible bands. The spectral distance from the SWIR to the visible bands is quite large, and the exponential extrapolation is not validated. The apparent discrepancy in the red channel could be partly attributed to the spectral distance between the channels on OLI (655 nm) and on the CIMEL / SeaPRISM instrument (667 nm) in a spectral region with important change in reflectance of turbid waters (Ruddick et al., 2006). No correction has been applied for the difference in band centre on the OLI and the CIMEL instruments: OLI bands are centred on 443, 483, 561, 655, and 865 nm, the CIMEL bands are 411, 441, 491, 530, 551, 667, 870, and 1019 nm.

The SD-MUMM performs similarly to VR2014, with lower values in the blue and higher in the green. The lower values in the blue may be caused by a more realistic aerosol extrapolation using the aerosol models in SeaDAS. Note that a default $\varepsilon = 1$ was used for both processors in Figure 3 and Figure 6. For the first two matchups, the SD-NIR processor generally shows a good agreement, with an overestimation in the green and slight underestimation in the blue. The SD-SWIR processor gives more variability over the images and is generally overestimating. For the last date SD-NIR matchups are good in the green, with some underestimation in the blue and red, SD-SWIR shows good matching in the red, but an overestimation in the blue and green.

No quality control as described in Zibordi et al. (2009) has been performed yet on the Aeronet-OC data. There is an additional potential uncertainty associated with local small scale variability and with the precision of the coordinates used for the tower. From the imagery itself, the tower location seems to be a few pixels off from the provided coordinates. On some images a turbid wake

can be seen associated with the offshore platform (Figure 7). However, the spatial variability derived from the imagery itself - the vertical bars on the OLI matchups (the 10-90 interpercentile range) in Figure 4 - is relatively low. The spatial variability in the SD-SWIR matchups is higher due to the per-pixel noise in the SWIR bands (and thus model selection).

5. CONCLUSIONS

The results presented here are a first test of the OLI processing implemented in SeaDAS/l2gen, and should be interpreted with care. As of now the aerosol model selection has not yet been extensively evaluated and tuned, and no vicarious calibration has been performed. The largest differences in the comparison between the SD and VR2014 processors can be attributed to the per-pixel varying aerosol model selection in SeaDAS, and the simplifications made in VR2014 (e.g. aerosol transmittances and extrapolation). As expected, SD-MUMM gives very similar results to the VR2014 processor, especially in the red band.

From the limited number of matchups with the Aeronet-OC station at MOW1, it appears realistic turbid water spectra can be derived from Landsat-8. The VR2014 processor gives consistently higher ρ_w in the blue bands than the SD-NIR and SD-MUMM processors. The green band is generally higher in the SD approaches, while the differences in the red band are smallest. The SD-NIR and SD-SWIR processors show good correspondence. The SD-SWIR generally overestimates and has a fairly large level of noise. The VR2014 has a similar performance across the three matchups, with a small overestimation in the visible bands. The VR2014-SWIR approach has a slightly larger over-estimation across all bands. These issues are likely related to sensitivities in aerosol determination and the extrapolation using Equation 1. It should be noted that a turbid wake associated with the measurement platform has been observed on Landsat-8 imagery, which could potentially influence the in situ measurements.

Landsat-8/OLI shows large potential for use in coastal applications. The OLI processor will be made publicly available in SeaDAS in the coming months. This will make the Landsat-8 data accessible to a wider ocean colour community, and user feedback will help improve the processor. The experience with OLI is a good preparation for the planned implementation of Sentinel-2/MSI in SeaDAS.

Acknowledgements
USGS/NASA are thanked for the Landsat-8 imagery. This work was performed for the FP-7 HIGHROC project (grant agreement n° 606797). Processing software was developed in the Belgian Science Policy Office JELLYFOR-BE project (SR/37/135).

6. REFERENCES

Bailey, S.W., Franz, B.A., Werdell, P.J., 2010. Estimation of near-infrared water-leaving reflectance for satellite ocean color data processing. Opt Express 18, 7521–7527.

Barsi, J.A., Markham, B.L., Pedelty, J.A., 2011. The operational land imager: spectral response and spectral uniformity, in: SPIE Optical Engineering+ Applications. p. 81530G–81530G.

Gordon, H.R., Wang, M., 1994. Retrieval of water-leaving radiance and aerosol optical thickness over the oceans with SeaWiFS: a preliminary algorithm. Appl. Opt. 33, 443–452.

Irons, J.R., Dwyer, J.L., Barsi, J.A., 2012. The next Landsat satellite: The Landsat Data Continuity Mission. Remote Sens. Environ. 122, 11–21.

Morel, A., Gentili, B., 1996. Diffuse reflectance of oceanic waters. III. Implication of bidirectionality for the remote-sensing problem. Appl. Opt. 35, 4850–4862.

Ruddick, K., De Cauwer, V., Park, Y.-J., Moore, G., 2006. Seaborne measurements of near infrared water-leaving reflectance: The similarity spectrum for turbid waters. Limnol. Oceanogr. 51, 1167–1179.

Ruddick, K.G., Ovidio, F., Rijkeboer, M., 2000. Atmospheric correction of SeaWiFS imagery for turbid coastal and inland waters. Appl. Opt. 39, 897–912.

Vanhellemont, Q., Ruddick, K., 2014. Turbid wakes associated with offshore wind turbines observed with Landsat 8. Remote Sens. Environ. 145, 105–115.

Vermote, E., Tanré, D., Deuzé, J., Herman, M., Morcrette, J., Kotchenova, S., 2006. Second simulation of a satellite signal in the solar spectrum-vector (6SV). 6S User Guide Version 3.

Zibordi, G., Holben, B., Slutsker, I., Giles, D., D'Alimonte, D., Mélin, F., Berthon, J.-F., Vandemark, D., Feng, H., Schuster, G., others, 2009. AERONET-OC: a network for the validation of ocean color primary products. J. Atmospheric Ocean. Technol. 26.

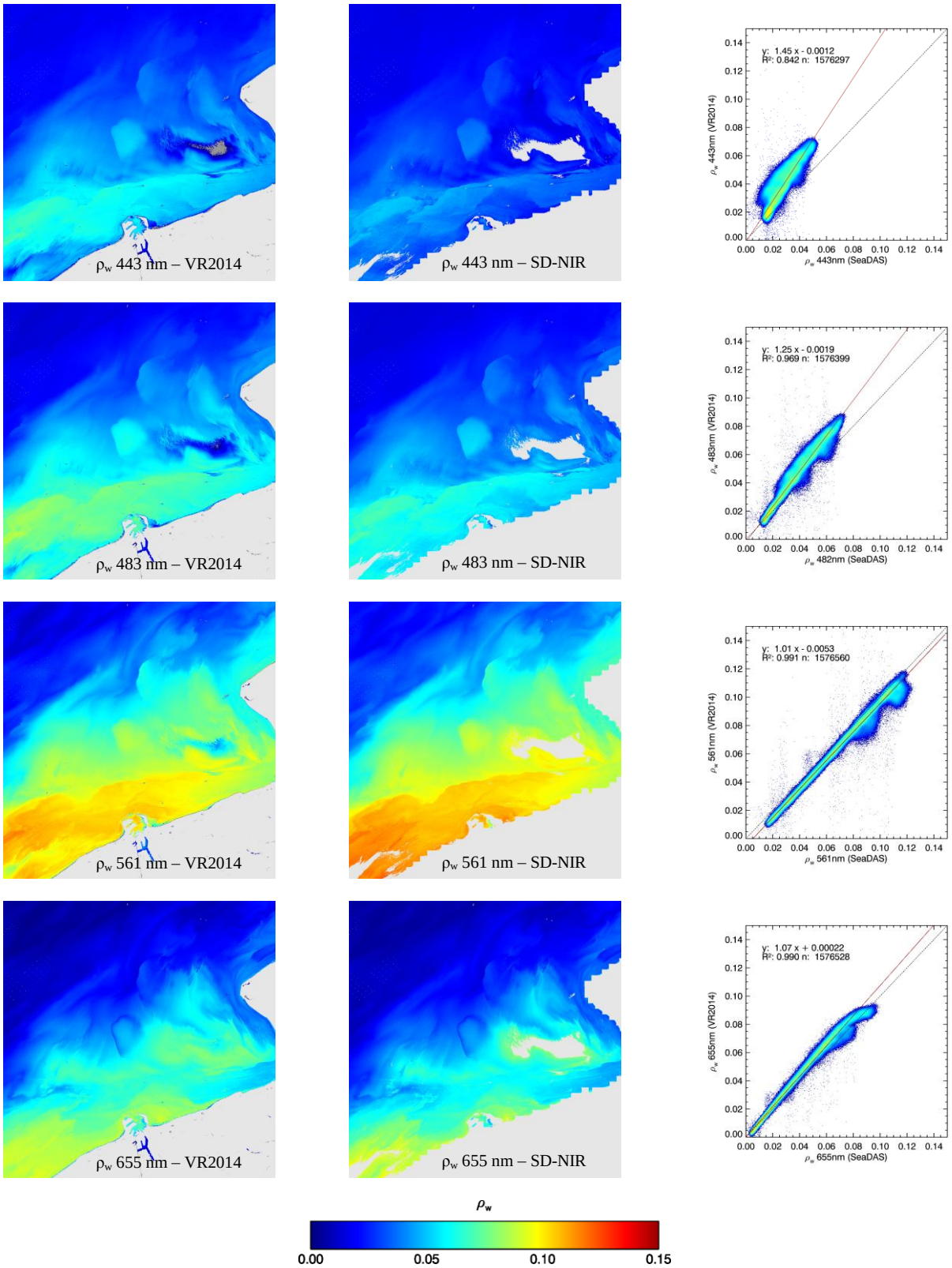

Figure 1 Marine reflectance (ρ_w) from Landsat-8/OLI for the 2014-03-16 (10:42 UTC) image, subset over Zeebrugge. Top to bottom: bands 1 through 4 (443, 483, 561 and 655 nm) and left to right: VR2014, SD-NIR processing and a scatterplot comparing SD-NIR and VR2014. Clouds, atmospheric correction failure and land are masked in light grey, negative values in dark grey.

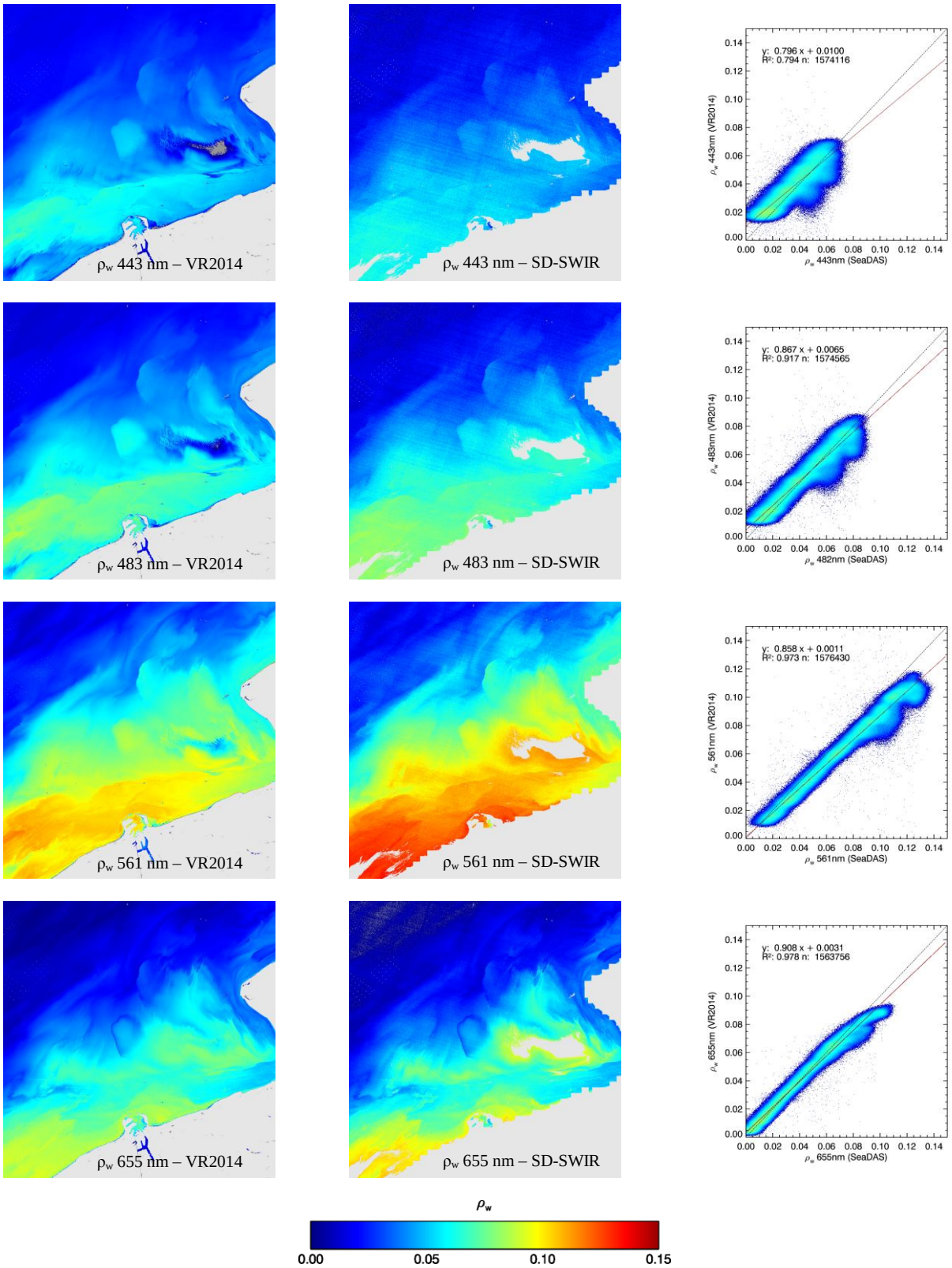

Figure 2 Marine reflectance (ρ_w) from Landsat-8/OLI for the 2014-03-16 (10:42 UTC) image, subset over Zeebrugge. Top to bottom: bands 1 through 4 (443, 483, 561 and 655 nm) and left to right: VR2014, SD-SWIR processing and a scatterplot comparing SD-SWIR and VR2014. Clouds, atmospheric correction failure and land are masked in light grey, negative values in dark grey.

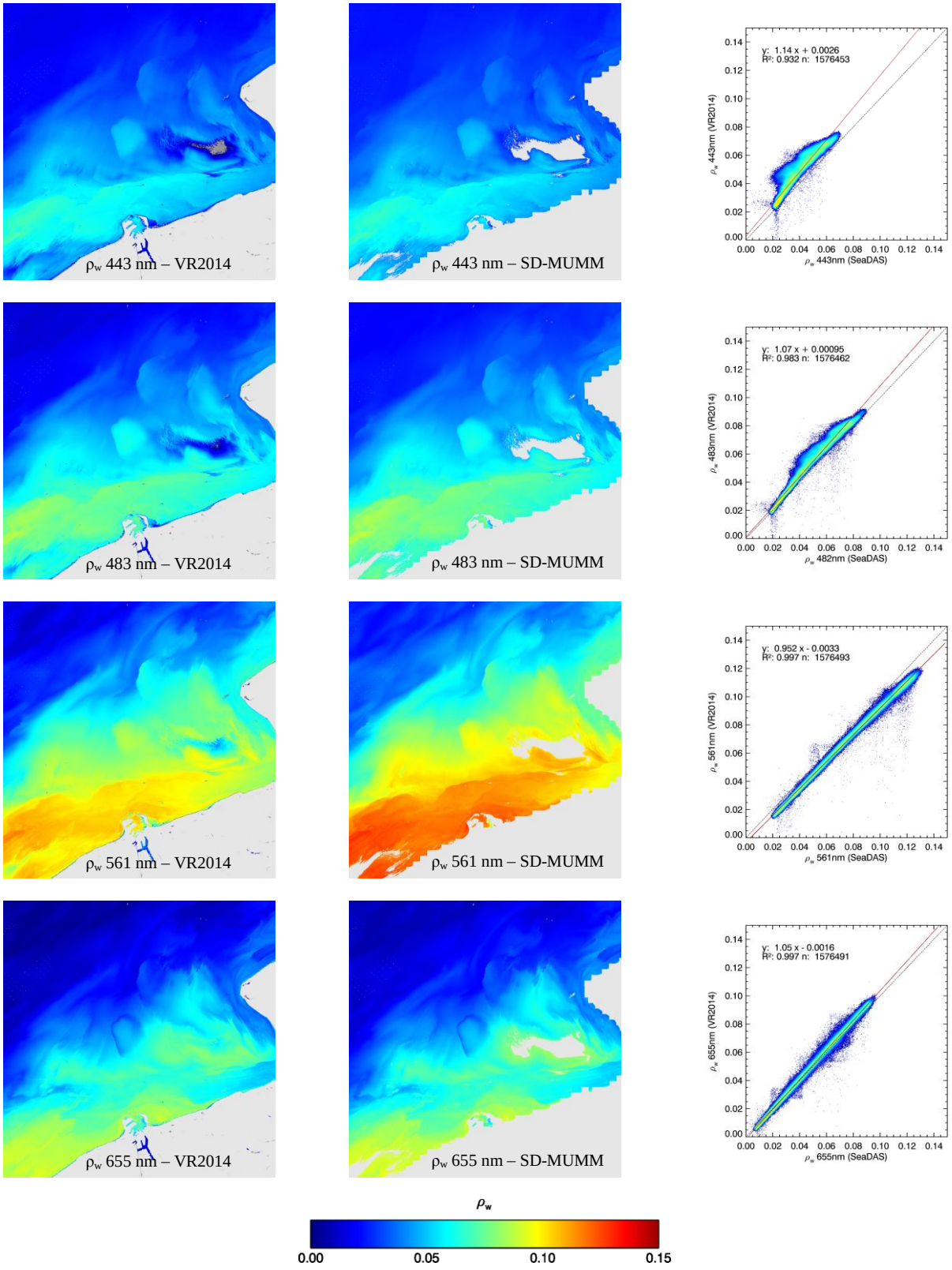

Figure 3 Marine reflectance (ρ_w) from Landsat-8/OLI for the 2014-03-16 (10:42 UTC) image, subset over Zeebrugge. Top to bottom: bands 1 through 4 (443, 483, 561 and 655 nm) and left to right: VR2014, SD-MUMM processing and a scatterplot comparing SD-MUMM and VR2014. In this comparison $\varepsilon = 1$ for both processors. Clouds, atmospheric correction failure and land are masked in light grey, negative values in dark grey.

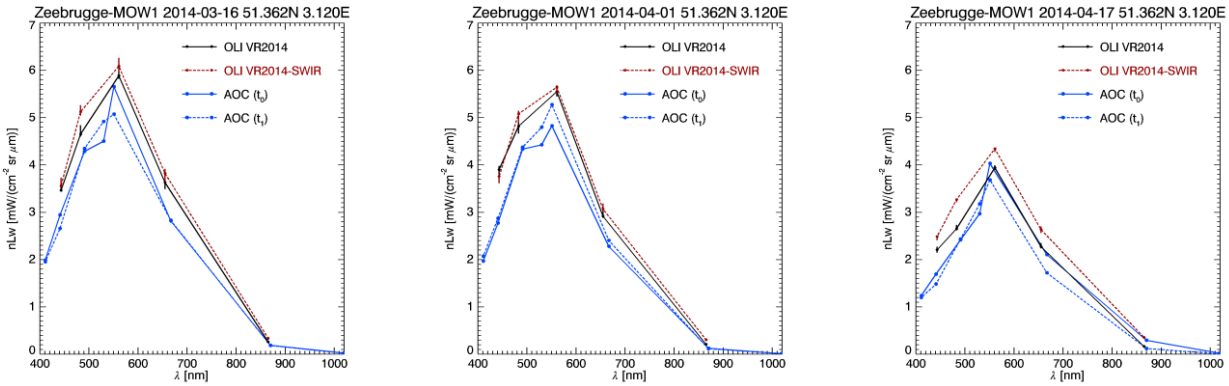

Figure 4 Normalised water-leaving radiance spectra from Landsat-8/OLI and the Aeronet-OC station at MOW1, left to right, 2014-03-16, 2014-04-01 and 2014-04-17. OLI spectra are plotted for the VR2014 (solid black) and VR2014-SWIR (dashed red) processing. The vertical bars on the OLI spectra denote the range between the 10th and 90th percentile within a 17x17 pixel box around the matchup pixel, corresponding to the spatial variability in a ~0.5 km pixel. Level 1 Aeronet-OC data is plotted, the closest matchup (t_0) in solid blue line, and the second closest matchup (t_1) in the dashed blue line.

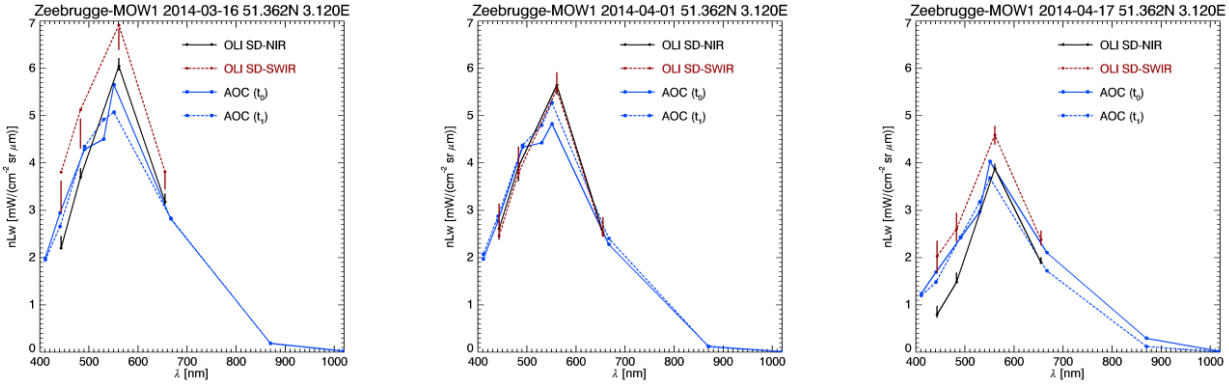

Figure 5 Same as Figure 4 but showing SD-NIR (solid black) and SD-SWIR (dashed red) processing. Spatial variability is larger in the SD-SWIR processing due to noise in the SWIR bands.

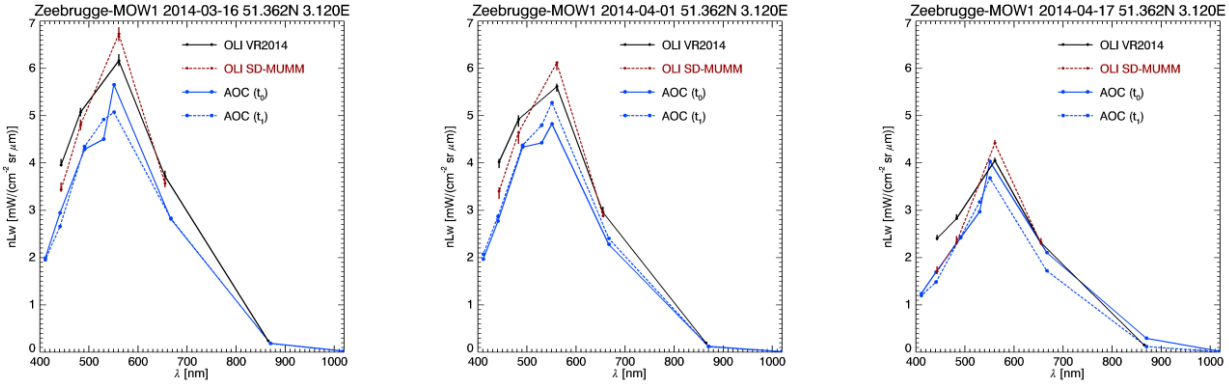

Figure 6 Same as Figure 4 but showing VR2014 (solid black) and SD-MUMM (dashed red) processing, both with $\varepsilon = 1$. Spatial variability is larger in the SD-SWIR processing due to noise in the SWIR bands.

Table 1 Bands of the Operational Land Imager (OLI) on Landsat-8, with wavelength range, ground sampling distance (GSD), signal-to-noise ratio (SNR) at reference radiance (Irons et al., 2012).

Band	Name	Wavelength (nm)	GSD (m)	SNR at reference L	reference L (W m^{-2} sr^{-1} μm^{-1})
1	Coastal/Aerosol	433–453	30	232	40.0
2	Blue	450–515	30	355	40.0
3	Green	525–600	30	296	30.0
4	Red	630–680	30	222	22.0
5	NIR	845–885	30	199	14.0
6	SWIR 1	1560–1660	30	261	4.0
7	SWIR 2	2100–2300	30	326	1.7
8	PAN	500–680	15	146	23.0
9	CIRRUS	1360–1390	30	162	6.0

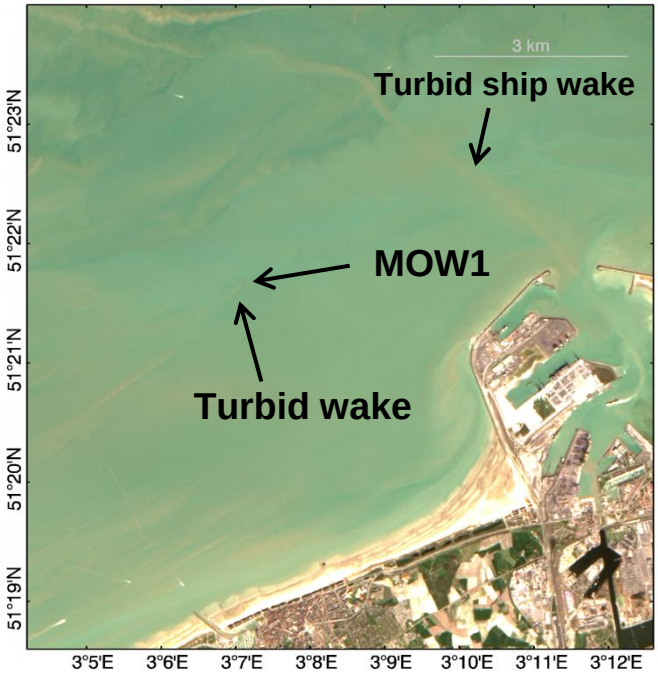

Figure 7 Pan-sharpened Rayleigh corrected RGB image for a subscene of the 2014-04-01 image, showing the eastern side of Zeebrugge harbour. The MOW1 Aeronet-OC platform can be seen, with an associated turbid wake.